Differential cross section for ω photoproduction measured in the Radphi experiment

Mihajlo Kornicer
Richard T. Jones
University of Connecticut, Storrs, CT

September 21, 2005

Abstract

The differential cross section for ω meson production in the reaction $\gamma p \rightarrow p\omega$, via $\omega \rightarrow \pi^0 \gamma \rightarrow 3\gamma$ decay, was measured using the Radphi detector. The data selection is discussed and the efficiency in the data collection and analysis is examined and quantified. The measured cross section as a function of beam energy and t, the square of the momentum transfered from the incoming photon to the outgoing ω, agrees well with previous results from ω photoproduction on a proton target.

1 Overview

The all-neutral $\omega \to \pi^0\gamma$ decay has been observed in the Radphi detector, where the ω is produced by a tagged photon beam in the energy range 4.4-5.4 GeV incident on a beryllium target. The ω yield is deduced from the 3γ invariant mass distribution. The yield is compared to that expected based on the known cross section for the $\gamma p \to p\omega$ reaction, under the assumption that the nuclear photoproduction cross section is given by the free nucleon cross section multiplied by the number of protons in the nuclear target. Any deviation observed between photoproduction cross sections on the free and bound nucleon would be evidence for nuclear medium effects in ω photoproduction.

The acceptance of the data collection is determined by the detector geometry and resolution, and by the trigger. The Gradphi Monte Carlo (MC) simulation program is used to estimate the detector acceptance and the offline reconstruction efficiency. The results reported below are based upon the complete Radphi data set of 10^9 tagged events collected in a run period of 450 hours of integrated live time. The integrated luminosity for tagged photon interactions during the experiment is $1.89 \cdot 10^7$ μb^{-1}. The trigger and offline analysis were devised to select events with a single charged track at lab polar angle greater than 30^0 so that peripheral γp interactions are the dominant source of ω production in this data set. The contribution from reactions involving neutrons in the target has been estimated based upon Monte Carlo simulations. The contribution from Δ and higher baryon resonance production is separated from diffractive production based on a missing momentum analysis.

2 Experimental Setup

The Radphi experiment used a tagged beam of bremsstrahlung photons produced by the continuous 5.6 GeV electron beam at Jlab. The experiment was designed to trigger on all-neutral final states produced in the beryllium target. The main components of the Radphi detector are shown in Fig. 1. The primary component was the lead-glass detector (LGD) used to measure multi-photon final states in the forward direction. The LGD was assembled as a circular array of 620 lead-glass blocks with a hole of 2x2 blocks in the center for the unscattered beam. The LGD was placed 1 m downstream from the target and covered lab polar angles from 3-28^0, with good shower reconstruction capability within a range 4-24^0. A 30-channel scintillator array (CPV) covering the entire angular region in front of the LGD (not shown in the figure) was used to veto charged particles in the forward direction. High rates in the CPV prevented its use in the on-line trigger so the vetoing of charged particles was applied during the off-line analysis. The angular region 30-100^0 with respect to the target was covered by a cylindrical barrel detector The barrel detector consisted of 3-layer scintillation hodoscope (BSD) surrounded by a lead-scintillating-fiber calorimeter (BGD). The BSD layers consisted of left-going and right-going spiral layers of 12 channels each, combined with the outer layer with 24 straight counters. A charged particle penetrating though all three layers produced a coincidence between a triplet of BSD channels whose overlap defined a space point known as a pixel. The BSD was used to trigger on a recoil proton from γp interactions, and the pixel information was used to determine the recoil proton direction. The BGD was segmented into 24 azimuthal segments, with the fibers running parallel to the beam direction. Photo-tubes in each end of the BGD modules recorded the time and position of particles in a barrel region. Sensitivity of the BGD was limited to a threshold of 20 MeV by the level of the electromagnetic background coming from the target. The BGD was used to detect photons emerging at large angles that cannot be detected by forward calorimeter.

Upstream of the target was a 10-cm thick lead shield wall with a 6.5 cm diameter hole for the photon beam. Just downstream of this wall was a 8-channel scintillator array (UPV) used to veto beam halo particles. The experiment was mounted in the alcove of Hall B at Jlab located 40 m downstream of the bremsstrahlung radiator and tagging spectrometer [1]. A helium tube filled a region between the tagger and the alcove to reduce beam interactions upstream of the detector. The experiment used only tagging counters 1-19 of the Hall B tagging spectrometer to tag photons with energies from 4.4-5.4 GeV, 75% to 95% of the electron beam energy. Using a gold bremsstrahlung radiator of thickness $3 \cdot 10^{-4}$ radiation lengths and electron beam current of $80\mu A$ produced a beam of approximately $5 \cdot 10^7$ tagged photons per second in this energy range. More details of the detector setup and performance are given in [2].

The experiment employed a three-level trigger to select all-neutral final states. The level-1 trigger was a coincidence between the logical OR of the signals from the photon tagger and the logical AND of the three layers of the BSD. The UPV scintillators were also included as an anti-coincidence at level-1. In the level-2 trigger at least one of the calorimeter modules in the LGD was required to be above a minimum
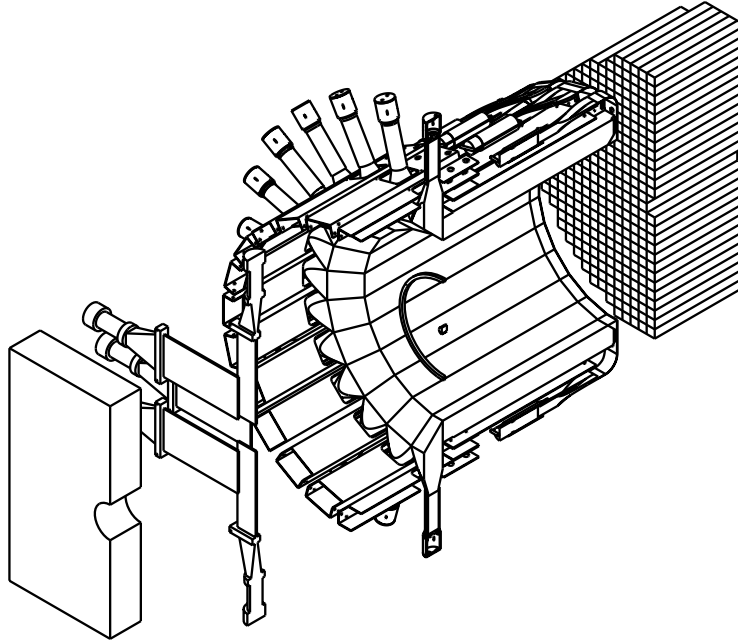
Figure 1: A cut-away view of the half of the Radphi detector. The beam enters the figure from the lower-left passing through a hole in the lead shielding wall (foreground) and strikes the beryllium target (small disk at the center of the figure) which is suspended by thin wires from an aluminum ring. Surrounding the target are the barrel scintillator detector (BSD) and barrel gamma detector (BGD). In the forward region is the lead glass detector (LGD) covering polar angles $3^0 - 28^0$. Immediately in front of the LGD was a scintillator plane (not shown in the figure) which functioned as a charged particle veto (CPV). The scintillator array in the foreground is the upstream particle veto (UPV). Approximately 40 m upstream of the target was the photon tagger (not shown), where photons with energy between 4.4 and 5.4 GeV were tagged.

threshold, which was set at 1 GeV. The level-3 trigger required that the sum of all LGD modules be above the threshold, set at 3.0 GeV. All events that passed level-3 were recorded to tape for off-line analysis.

3   Event Reconstruction

In the off-line analysis the overlap geometry of the three BSD layers enabled a unique identification of a space point (pixel) along a track of a charged particle based upon a triple coincidence between the layers. After adjusting for light propagation, a pixel time was formed to estimate the start time for the event, which was used as a common reference time for all other detector components.

A photon incident on the LGD deposits energy in several LGD blocks. The first step in event recon-struction was to go down the list of all blocks with energy above pedestal and to group adjacent blocks into clusters. The summed energy for each cluster and the cluster centroid were used to estimate photon energy and direction using a 2-dimensional non-linear response functions that ware derived from Monte Carlo (MC). Photon showers from 50 MeV up to 5 GeV were effectively reconstructed in the LGD. Most of the photons below 50 MeV consisted of a single LGD block and could not be distinguished from noise. In the case where two showers appear close together in the LGD, the energy of the blocks common to both clusters was shared using an algorithm that depended upon the distance of the block from each adjacent cluster and the cluster energies. The minimum cluster separation was 6 cm, limited by the dimension of the LGD block of 4 cm. Consequently, photons closer than 6 cm at the face of the LGD were merged into a single cluster. The LGD segmentation allowed this clusterizer to effectively reconstruct events of shower multiplicities up to 8.

The initial calibration of the LGD was done by adjusting the HV of the LGD photo-tubes to equalize the response of the optical light pulse from the UV laser that was fanned-out to all of the blocks. Off-line, the energy calibration of the LGD was refined by constraining the 2γ invariant mass in 2-cluster reconstructed events to match the physical mass of the π^0. In the class of events with two reconstructed showers the π^0

peak dominates the invariant mass spectrum. All events with an invariant mass within $\pm 30\%$ of the π^0 mass were selected, and the global χ^2 for the sample was computed reflecting the width of the π^0 peak. This χ^2 has quadratic dependence on the individual gains of each LGD channel, permitting the iχ^2 to be minimized in respect to gains by solving a linear equation [2]. The adjusted gains were used in repeated passes through the reconstruction until the gain corrections converged to fixed values. This procedure lead to a final π^0 peak whose width match the one obtained by reconstructing MC simulated events with ideal calibration. The calibration was checked by examining other known all-neutral meson decays: $\eta \rightarrow \gamma\gamma$ in the 2-cluster sample, $\omega \rightarrow \pi^0\gamma$ in the 3-cluster sample and $\eta \rightarrow 3\pi^0$ in the 6-cluster sample. The single-shower spatial and energy resolutions of the LGD extracted from the widths of the π^0 and η mass peaks ware in good agreement with expectations for lead glass calorimeters [3]. More details regarding event reconstruction, detector calibration and resolution can be found in [2]

4   Data Selection

The following criteria ware used to select a clean ω sample:

1. 0.05 GeV minimum shower energy in the LGD,

2. exactly three showers reconstructed in the LGD,

3. 3.0 GeV minimum total shower energy in the LGD,

4. only one pixel cluster in the BSD,

5. no coincident hits in the forward veto scintillators (CPV),

6. no showers reconstructed in the barrel gamma detector (BGD),

7. no low-energy showers around the beam hole in the LGD,

8. kinematic selection of $\pi^0\gamma$ events.

The minimum shower energy cut (1) suppresses electromagnetic background in the calorimeter. Cut 2 selects most of the $\omega \rightarrow \pi^0\gamma$ decays that appear in the Radphi sample. Some of these decays also feed into the four-shower sample, which will be discussed later. Cut 3 refines total energy cut that was made by the on-line level-3 trigger after the off-line energy calibration has been applied. Cut 4 applies a single recoil track requirement that corresponds to events with 1-prong in the barrel region. An event is classified as n-prong if there are n charged tracks coming from the primary reaction vertex. The cut 4, combined with the forward charged particle veto (5), rejects multi-prong reactions, which dominate the total photoproduction cross section at these energies. The barrel gamma veto (6) rejects events with large angle showers as well as suppressing several reactions with an excited baryon in the final state. The beam hole cut (7) is needed to reduce a contamination from uncorrelated photons around the beam hole that result from the electromagnetic interactions of the beam in the target. The selection of events with $\pi^0\gamma$ kinematics (8) further improves the ω signal-to-background ratio.

The charged particle veto cut (5) was very important because of the high rate of multi-prong reactions that dominate over the one-prong final states that are the focus of study in this analysis. The total rate observed in the CPV was a factor of about 300 larger than the calculated total photo-nuclear interaction rate in the target, indicating that that the CPV is dominated by electromagnetic backgrounds. MC simulations were able to reproduce the observed rates in the CPV within 5% based on electomagnetic interactions alone. Because of these high rates, dead-time considerations prevented the use of the CPV in the on-line trigger. The coincidence spectrum between the CPV and a BSD pixel is shown in the first panel of Fig. 4. The peak near $\Delta t = 0$ comes from CPV-BSD coincidences which sits on top of a large background coming from accidentals. The veto window of 6 ns width, indicated by the dashed lines in the figure, was chosen as a compromise between veto efficiency (95%) and signal loss from accidental vetoes (32%).

Identification of a given reconstructed event with a single tagged photon is not possible because of the high rates in the tagger $(5 \cdot 10^7 s^{-1})$. A tagged photon spectrum is formed by requiring a coincidence between a tagging counter and the BSD pixel that defines an event, and then subtracting the accidental component using the delayed-coincidence technique. This method is illustrated in the second panel of Fig. 4. The solid histogram shows the time difference spectrum between the tagger and a BSD pixel. The regular spikes in
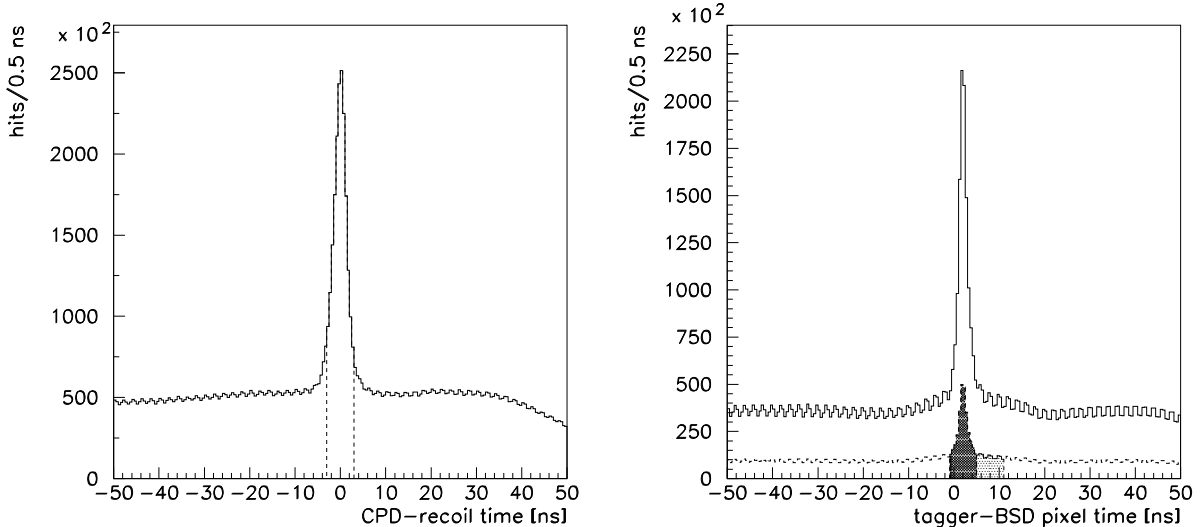
Figure 2: The time difference between a pixel and a hit in the CPV (left) and the tagger (right). Dashed lines in the left panel show the time window used for the charged particle veto. The right panel shows the tagger-pixel time difference before (solid) and after (dashed) the CP veto is applied. The shaded areas in the right panel show the time windows used for counting tagger coincidences (peak region) and accidentals (right of peak region).

the spectrum reflect the 2 ns substructure of the CEBAF beam. The dashed histogram results when the CP veto is applied to remove all pixels associated with forward-going charged tracks. The shaded area under the peak shows the pixels which are identified with tagged coincidences, while the shaded area to the right of the peak indicates those that are used for accidentals subtraction.

5   Invariant mass spectra

There are $2.47 \cdot 10^8$ events that ware reconstructed with three showers in the LGD. The effects of various cuts on the 3γ invariant mass spectrum are shown in Fig. 3. The left plot in Fig. 3 is obtained from the full sample after the application of cuts 1-4. The solid line in the right plot of Fig. 3 shows the effects of cuts 5 and 6, while dashed line shows the effect of cut 7. After these three additional cuts the peak around 0.8 GeV/c^2 that is associated with $\omega \rightarrow \pi^0 \gamma$ stands out clearly above the background. The peak below 0.2 GeV/c^2 arises from a solitary π^0 that feeds into the 3γ sample by the addition of an accidental low-energy shower. Similarly, the peak around 0.6 GeV/c^2 is associated with feed-through from a solitary $\eta \rightarrow 2\gamma$ decay. MC simulations show that the enhancement around 0.35 GeV comes from leakage of multi-prong events into the sample [4], mainly $\rho^- \rightarrow \pi^- \pi^0$ and $\omega \rightarrow \pi^- \pi^+ \pi^0$, where one of the charged pions deposits enough energy in the calorimeter to mimic a low energy shower.

A method that is effective for reducing feed-through from 2γ channels is to require that the invariant mass of the lightest photon pair in the final state falls in the region of the π^0 peak. Fig. 4 shows the 2γ invariant mass of all pairs from the 3γ sample (solid line) and the lightest pair (dashed line). Accidental background showers tend to produce events with at least one photon pair with a mass less than 100 MeV/c^2. Requiring the lightest pair to have a mass between 0.1 and 0.18 GeV (cut 8, shown by dotted lines in Fig. 4) effectively suppresses those events while preserving essentially all of the $\omega \rightarrow \pi^0 \gamma$ signal.

The last analysis step is to apply the tagging coincidence requirement and subtract tagging accidentals. The final result for the 3γ invariant mass spectrum is shown in Fig. 5, left panel. The histogram is fitted with a sum of two Gaussians and one forth-order polynomial (solid curve). The larger Gaussian represents the ω meson, while the smaller one corresponds to the remnants of the η. The sum of the η Gaussian and polynomial function, representing the hadronic background, is shown by the dashed curve. The ω yield from the fit, the peak position, the width and the signal-to-background ratio are listed in the first row of Table
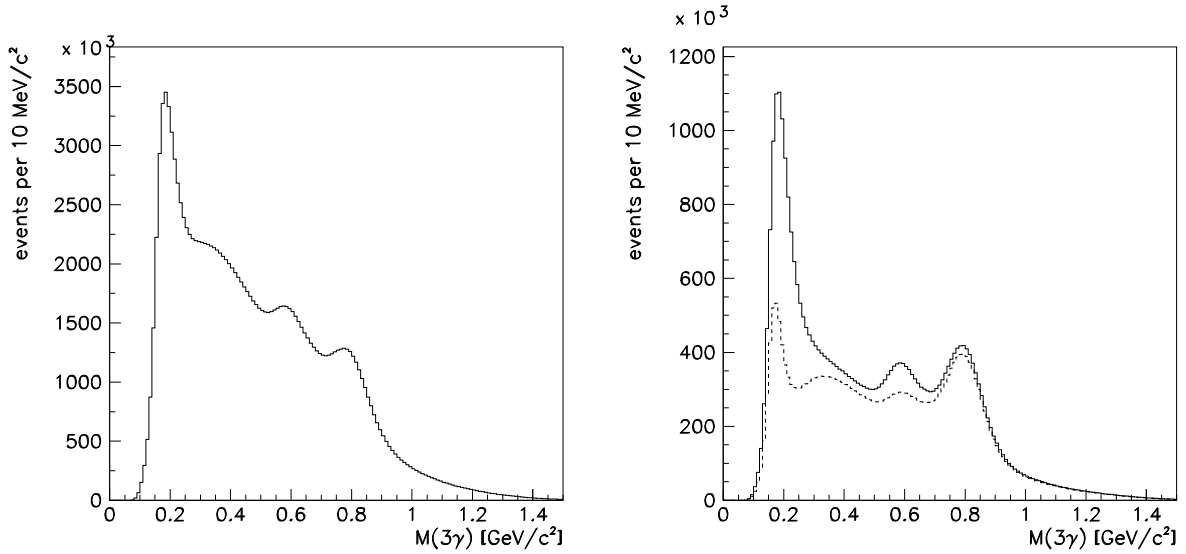
Figure 3: The invariant mass distribution from the 3γ sample obtained after cuts 1-4 (left panel), after cuts 1-6 (right panel solid curve) and after cuts 1-7 (right panel dashed curve).
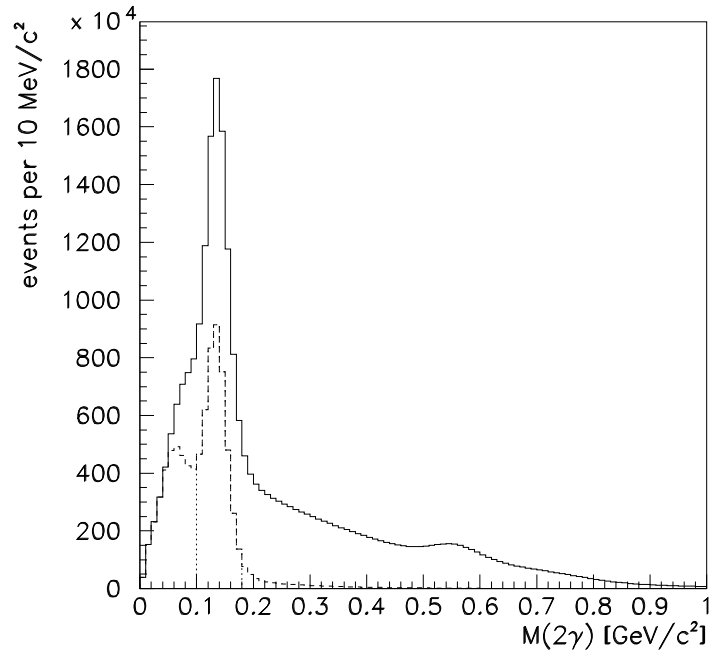

Figure 4: The invariant mass distribution of all photon pairs from the 3γ sample (solid line). The dashed line corresponds to the lightest pair. The vertical dotted bars show the limit imposed by cut 8. Eliminating events with the lightest pair mass below 0.1 MeV/c^2 effectively removes $\gamma p \rightarrow \pi^0 p$ events that leak into the 3γ sample through the addition of a low energy background cluster.
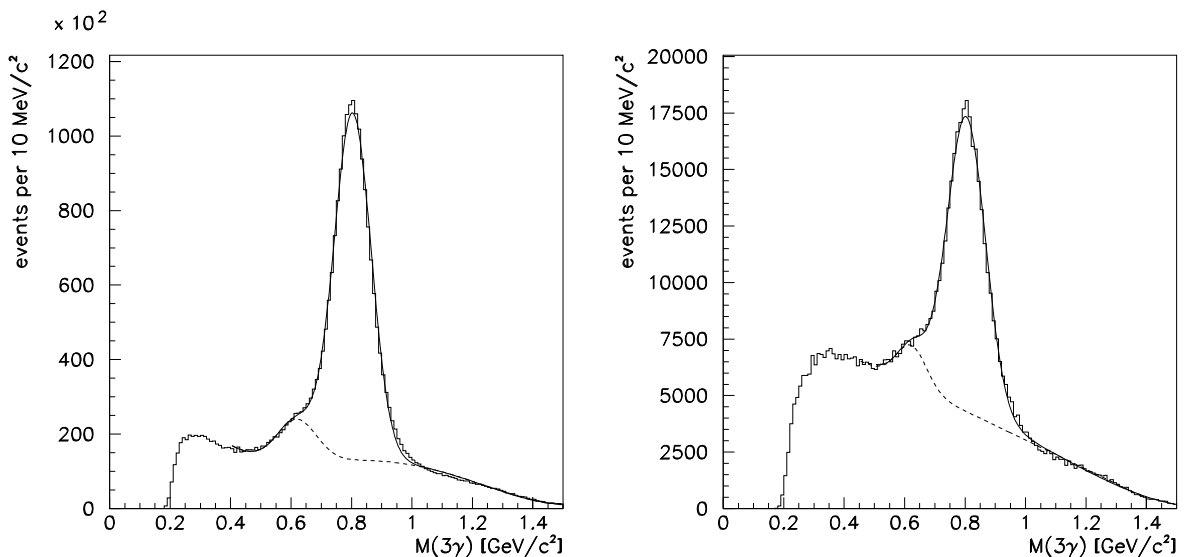
6

Figure 5: The 3γ invariant mass distribution for the final 3γ sample (left) and 4γ sample (right) after applying cuts 1-8 and applying the tagger coincidence.

Table 1: Results of fitting the 3γ invariant mass distributions from the sample with 3 and 4 reconstructed showers. Reported errors are dominated by systematics associated with a choice of the background parametrization.

sample	Yield [10^6]	Mean [GeV]	σ [GeV]	$\frac{Signal}{Background}$
3γ	1.50±0.08	0.789±0.002	0.062±0.002	6.1
4γ	0.24±0.02	0.784±0.002	0.066±0.003	2.5

1.

   In a similar fashion to the way 2γ events feed-through into the 3γ sample, a significant fraction of the $\omega \rightarrow \pi^0 \gamma$ signal leaks in the 4γ sample. Many of these can be recovered using cut 7 to remove a low energy shower near the beam hole. Once this shower is removed, the event is analyzed in exactly the same way as the 3γ sample. Final results following from this procedure are shown in Fig. 5 (right panel) and Table 1 (second row).

   As a result of merging of showers with small angular separation, a weak ω signal was observed in the 2-shower sample as well. The same effect was seen in MC simulations. The loss of the ω signal through feed-down in shower multiplicity was taken into account in computing the MC acceptance.

6 Cross section normalization

The integrated luminosity for the experiment is the product of the total tagger count with the tagging efficiency and the target thickness. The total tagger count was monitored by scalers on the individual tagging counters. Their sum was corrected for dead time using the ratio of gated and ungated trigger scalers. The tagging efficiency is defined as the number of tagged photons incident on the target divided by the sum of the tagger scalers. As such, it is a product of a geometric factor and an electronic factor. The geometric factor is the number of tagged photons striking the target per hit in the tagger focal plane. The electronic factor takes into account the fact that the tagger scalers count somewhat faster than the rate of electrons hitting the focal plane. This arises from double-firing discriminators and electrons that produce signals in more than one focal plane counter. The electronic factor is measured by analyzing the tagger time spectra on a run-by-run basis. The geometric factor is calculated from the bremsstrahlung differential cross

Table 2: The widths and relative contributions of the two Gaussians that describe the out-of-plane recoil proton momentum distribution seen in the real data, compared with that seen in reconstructed MC. In the MC events the out-of-plane recoil proton momentum distribution is controlled by the initial state nuclear momentum distribution described by a sum of two Gaussians parametrized as shown in the last row. The parameters of that distribution were adjusted to obtain a good agreement between the reconstructed MC and the real data. Given errors are statistical only.

	σ_1 [MeV]	f_1	σ_2 [MeV]	f_2
data	110.0±0.5	0.615±0.004	246.±1.	0.385±0.006
MC reconstructed	110.±1	0.62±0.01	250±3	0.38±0.02
MC generated	100	0.55	400	0.45

section, with corrections for beam-target misalignment, which will be described later. The total luminosity for the experiment obtained in this way was 18.9 ± 0.4 pb^{-1}.

To estimate the acceptance of the on-line trigger and the off-line analysis a MC simulation was employed. Events were generated assuming $\gamma p \to \omega p$ kinematics. The initial-state momentum of the target proton was smeared according to a spherically symmetric nuclear momentum distribution described by the sum of two Gaussians. The widths of the two Gaussians and their relative weights were adjusted to make the out-of-plane recoil proton momentum distribution match that seen in the real data. The scattering plane is defined by the incident beam direction and the total momentum of the 3γ system in the final state. For a free nucleon target the recoil proton momentum is constrained to lie in this plane by momentum conservation but in a case of a nuclear target the Fermi motion of the initial-state proton in the nucleus results in an out-of-plane component. The parameters that describe the nuclear momentum distribution are given in Table 2. A spectator model in which the outgoing proton does not interact with the residual A-1 nucleon system in the final state was used to generate the recoil proton momentum. The ω was generated with zero net polarization and decayed into $\pi^0 \gamma$ with a branching ratio of 8.92%. The angular distribution of the ω in the center-of-mass frame of the reaction was specified by an exponential t-distribution. The generated t-slope was adjusted to agree with that seen in real data for the range $0.3 < |t| < 1.0$ GeV^2, as described below. Events thus generated were simulated using the Geant-based program $Gradphi$ which converted the input kinematics into hits in the detector elements. The simulated events were subjected to the on-line trigger requirements followed by the same off-line analysis as described in the preceding section for real data.

Figure 6, left panel, shows the t-distribution for the 3γ ω sample. In the $|t|$ range of $(0.3, 1.0)$ GeV^2 the real data distribution is overlaid with by an exponential function e^{bt} with the slope parameter $b = 5.7$. The same slope in MC reconstructed data is obtained using $b = 5.5$ in the MC generator. The acceptance function for the reaction $\gamma p \to \omega(\pi^0 \gamma)p$ based upon a sample of 50M generated events, is shown in the right panel of Fig. 6. Errors shown in the plot are statistical only. Fig. 7 shows the mean and RMS of the reconstructed t as function of generated t. The solid line in the left plot marks $t_{rec} = t_{gen}$, showing that the bias in reconstructed t is negligible.

The average MC acceptance of the detector was obtained by dividing the total number of reconstructed ω events by the number generated. Its value is listed in Table 3, together with its systematic error. The error includes uncertainties arising from the choice of various tunable parameters in the MC generator and in the detector response model used by the simulation.

The beam-target misalignment is estimated by analyzing the azimuthal distribution of the scattering plane. This distribution for 3γ events with invariant mass in a range $0.7 < M(3\gamma) < 0.9$ GeV is shown in the left panel of Fig. 8. Any shift of the beam from the geometric center of the target is expected to produce an azimuthal asymmetry because of the varying amount of material seen by the recoil proton as it exits the target. To quantify this effect the beam-target displacement was varied in the simulation and the azimuthal asymmetry compared with that seen in real data. The final distributions are shown in Fig. 8, where MC distribution is obtained by shifting the beam by 5 mm in the direction of x-axis. Both distributions are fitted with the function

$$Y(\phi) = A + B\sin(\phi + C) \tag{1}$$

with A, B, and C being fitting parameters. The fits are shown by solid curves in Fig. 8. The flat dashed lines represent the case where the beam spot is centered on the target. The deviation from a sinusoidal shape seen in the real data between 75^0 and 135^0 is related to the non-uniform efficiency of a few BSD counters in
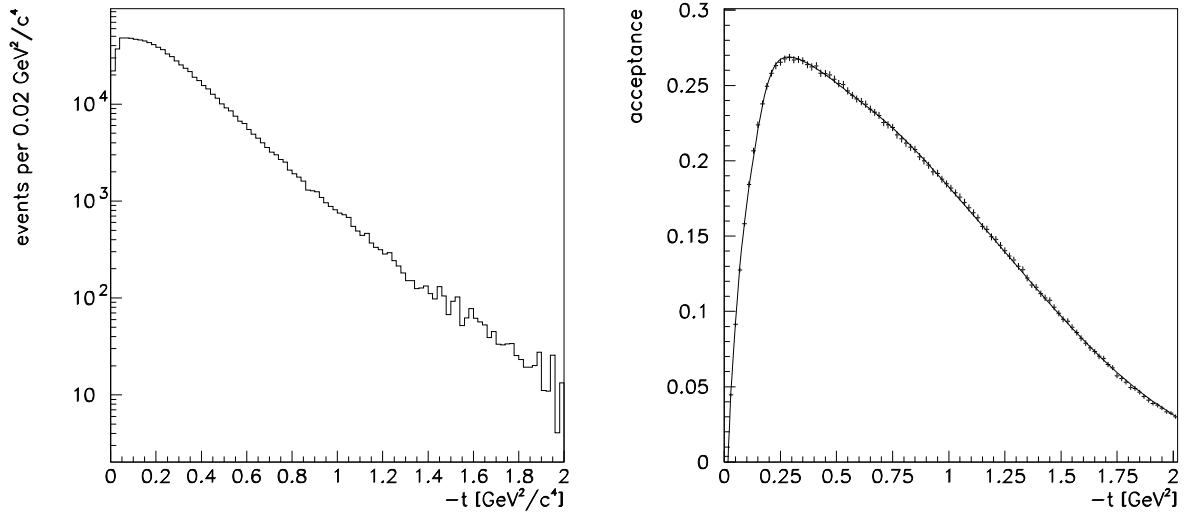
8

Figure 6: The t-distribution from the 3γ ω sample (left), and MC-acceptance (right).
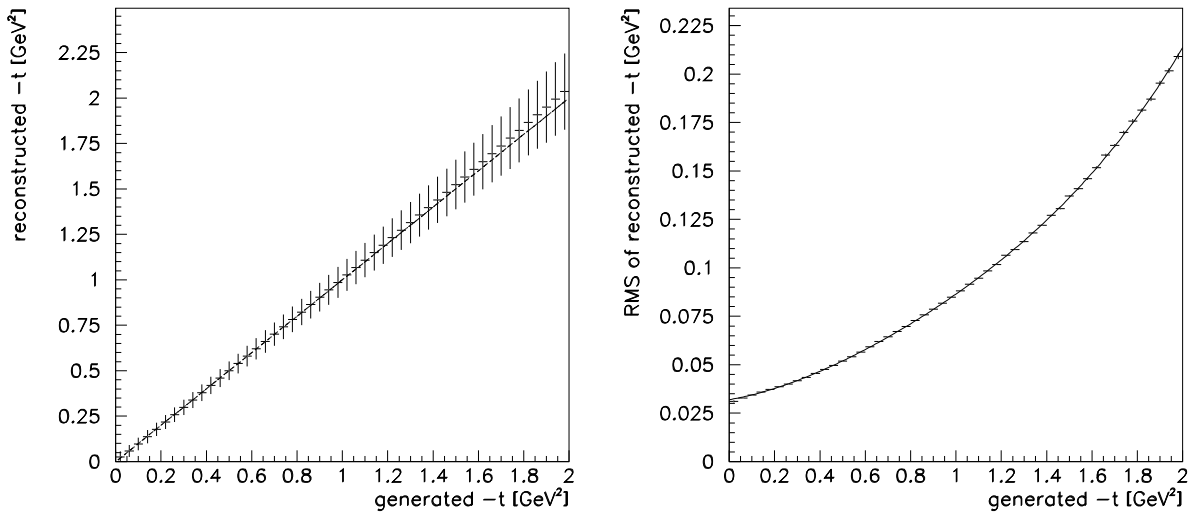

Figure 7: The mean and RMS of the reconstructed t as function of generated t obtained with the MC simulation. The left plot shows the centroid and width in the form of error bars, while the right plot shows the width separately.

Table 3: The total ω yield measured from 3γ and 4γ samples, cross section normalization factors and total ω photoproduction cross section. The acceptance assumes an exponential t-distribution with a slope $b = 5.5$. This cross section includes contribution from Δ and N^* resonances as well as diffractive ωp production.

ω yield $[10^6]$	1.74±0.09
B.R.$(\omega \to \pi\gamma)$	0.089±0.003
luminosity $[pb^{-1}]$	75.6±1.5
acceptance	0.18±0.01
pixel efficiency	0.70±0.03
CPV accidentals	0.68±0.01
$\sigma[\mu b]$	3.0±0.2

that range. A beam shift of 5 mm with respect to the target center produces a 4% reduction in the tagging efficiency. This geometrical correction to the tagging efficiency is included in computing the total luminosity reported in Table 3. The luminosity in Table 3 includes a factor of 4 coming from the number of protons in the target nucleus. The systematic error on the luminosity is mainly associated with the ±1 mm uncertainty in the beam-target misalignment derived from the MC procedure described above.

Also included in Table 3 are two experimental acceptance factors which are not accounted for by the simulation, but are directly measured. The BSD pixel efficiency is defined as the probability that a charged particle passing through all three BSD layers will result in a triple coincidence (pixel) between overlapping counters in the tree layers. The efficiency in a single layer is only about 90% because on-line thresholds were set somewhat high in order to provide some discrimination between protons and EM background. The pixel efficiency is computed as the product of the efficiencies of the three individual layers. The individual layer efficiencies are measured by requiring a hit in two of the three layers, and counting the fraction of times that the third layer fired. Because all of the recorded events ware required by the trigger to have at least one hit in each layer, this measurement suffers from a trigger bias. This bias is reduced for events with larger numbers of pixels because the trigger is satisfied by *any* hit in all three layers. The layer efficiency measurement was repeated while selecting events with variety of pixel multiplicities m, and the systematic error was assigned based on the uncertainty of extrapolation to large m.

The remaining experimental acceptance factor accounts for accidental CP vetoes. The total rate in the CPV was approximately 75 MHz. That rate, combined with the veto time window of 6 ns, leads to an accidental fraction of 64%, assuming that all of the hits in a CPV plane are uncorrelated. However we know that in some cases CPV hits come together in pairs or higher multiplicities. The only reliable way to extract the accidental veto rate from the data is to count the ω yield before and after the veto has been applied. Uncertainties in integrating the ω mass peak under the different background conditions before and after the veto leads to the systematic error shown in Table 3 for the accidental CPV lost fraction.

Taking into account all normalization factors the total ω photoproduction cross section, given in Table 3, is obtained. This cross section contains a dominant contribution from the reaction $\gamma p \to \omega p$ but also includes contributions from reactions of the type $\gamma p \to \omega N^*$ where N^* is an excited baryon resonance. The isolation of the contribution of $\gamma p \to \omega p$ from N^* reactions is discussed in the next section.

7   Contributions from N^* production

The trigger and off-line analysis were devised to select final states with a recoil proton. However, the acceptance for reactions with an excited recoil baryon is significant. For example, MC analysis shows a relatively large reconstruction probability for reactions where the ω is produced opposite a Δ^0 or Δ^+, while the reconstruction probability for the reaction $\gamma n \to \omega n$ is negligible. The reactions with highest acceptance involving Δ production are $\gamma p \to \omega(\pi^0\gamma)\Delta^+(\pi^+n)$ and $\gamma n \to \omega(\pi^0\gamma)\Delta^0(\pi^-p)$, with respective acceptances of 10% and 7.4%. In the first reaction the π^+ substitutes for the proton in the recoil trigger. In the second reaction one of the charged particles is identified as a recoil while the other goes undetected.

In any case, the ω signal seen in the 3γ invariant mass spectrum is the same regardless the type of baryon produced with it. One way to suppress the resonance contribution to the measured cross section would be to apply a cut on the total energy of the forward system with respect to the incident photon energy. For example a 500 MeV cut in the difference between the total shower and tagger energy reduces the
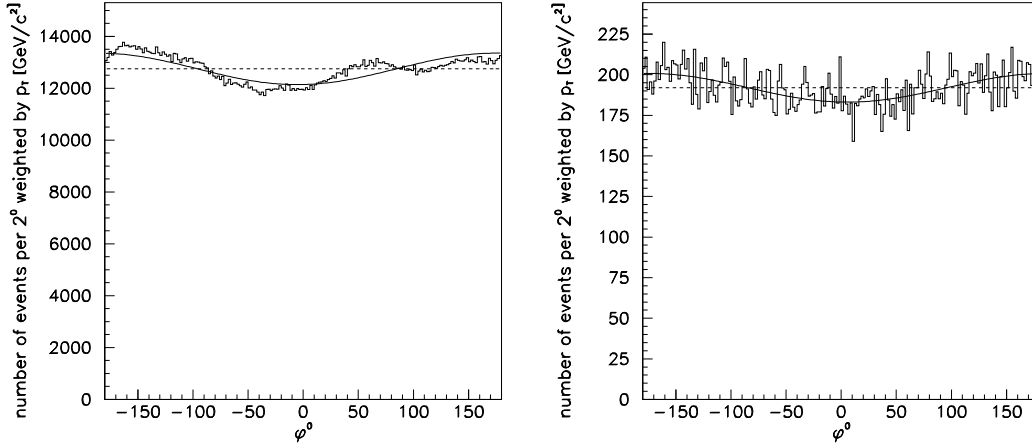
Figure 8: Azimuth distribution of the transverse momentum of the forward 3γ system with invariant mass $0.7 < M(3\gamma) < 0.9$ GeV (left) and from MC when the beam is displaced by 0.5 cm in the direction of x-axis (right).

acceptance of ω reconstruction from Δ reactions by about 60%. However, this cut does not eliminate the resonance contribution completely, and the residual N^* contribution to the cross section remains uncertain. One observable that can be used to estimate the residual contribution is the distribution of the azimuthal angle $\Delta\phi$ between the recoil plane and the scattering plane. The recoil plane is defined by the incident beam direction and the direction of the recoil track. In the left panel of Fig. 9 are shown MC $\Delta\phi$ distributions from $\gamma p \rightarrow \omega p$ (solid), $\gamma p \rightarrow \omega\Delta^+(\pi^+n)$ (dashed), and $\gamma n \rightarrow \omega\Delta^0(\pi^-p)$ (dotted) reactions, normalized to the same number of reconstructed events. The intrinsic detector resolution in $\Delta\phi$ is 8^0. Even with nuclear Fermi motion broadening the central peak, one can see a clear difference between the shapes from diffractive and resonance production In the right panel of Fig. 9 is shown the $\Delta\phi$ distribution for real data, including only events within the ω peak. Events from narrow bands above and below the ω peak in the invariant mass spectrum have been subtracted in making right plot in Fig. 9 Even after this background is subtracted significant tails are seen outside the diffractive peek in the $\Delta\phi$ distribution which is interpreted as the N^* contribution. This distribution is fitted to a sum of the MC shapes shown in the left panel. Because d+ and d0 channels are isospin mirrors their cross sections are expected to be equal so their coefficients are locked together in the fit by the ratio of their acceptances. The $\Delta\phi$ fit (solid line in Fig. 9 right panel) reveals a net 22% contribution from rezonance channels (dashed line in Fig. 9 right panel). Although the analysis assumed only Δ production, this estimate also includes contribution from higher N^* resonances because they all exhibit a similar defuse $\Delta\phi$ distribution. A small part of the $\Delta\phi$ tails may also come from events with missing particles in the forward region, from reactions where the ω is the decay product from a heavier meson. But such events in MC simulations have much lower acceptance than the leading ωN^* production reactions.

8 Total and differential cross sections

The left panel in Fig. 10 (black points) shows the total ω photoproduction cross section measured by the Radphi as a function of the tagged photon energy, after the non-diffractive component has been subtracted. The 500 MeV cut on the difference between the total shower and tagger energy has been applied in addition to the cuts described in sections 2 and 3. This cut does not have a big impact on the mass spectrum but reduces the non-diffractive contribution to 10%, independent of beam energy. The Radphi ω photoproduction cross section agrees well with early measurements shown as solid [5] and open [6] squares.

To investigate the dependence of the differential cross section on incident photon energy, the differential cross section $d\sigma/dt$ has been fitted to an exponential form Ae^{bt} for each photon energy. Side-band subtraction in invariant mass plot has been used to produce t distributions that accurately reflect the ω signal seen in a
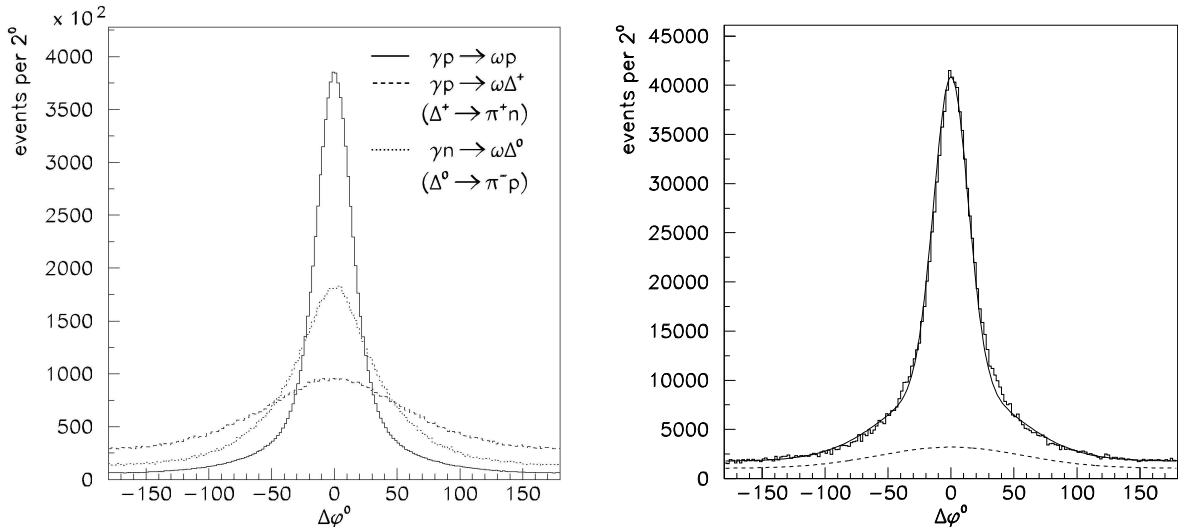
Figure 9: $\Delta\phi$ distributions from various MC reconstructed reactions (left panel) and from the real 3γ sample (right panel). The distribution on the right is fitted by the sum of the three MC distributions shown on the left. The fit is represented by a solid line and the sum of the resonance contributions is shown by the dashed line.

mass plot. The fit results for the b parameter as a function of incident photon energy are shown in Fig. 10 right panel. The b parameter is almost independent of energy within the displayed errors, which represent the systematic error associated with the choice of the fitting range in $-t$, 0.2-0.7 GeV^2 for the presented results.

Fig. 11 shows the differential cross section for ω photoproduction as a function of $-t$. To form this plot data from all tagged photon energies shown in Fig. 10 have been summed. The vertical error bars reflect the statistical error while horizontal errors indicate the bin size. Data from an older experiment [6] are shown as open symbols while newer data from CLAS [7] are shown as solid points (3.29 GeV incident photon energy) and squares (3.83 GeV incident photon energy). Overall agreement between the different data sets is observed. At very low $-t < 0.2$ GeV^2 the Radphi data show depletion in the differential cross section, compared to experiments performed on a hydrogen target. Such an effect is expected because of nuclear final state interactions. The exponential slope parameter $b = 5.5 \pm 0.4$ GeV^{-2} is obtained by fitting the differential cross section within the range $0.2 < -t < 0.7$ GeV^{-2}. This value is smaller then the previous result $b = 7.1 \pm 0.9$ GeV^{-2} obtained for the range $0.06 < -t < 0.5$ GeV^2 at a photon energy of 4.7 GeV [6]. However it is consistent with the CLAS measurement of 5.4 ± 0.6 GeV^{-2} at 3.6 GeV [7], given that b does not appear to vary rapidly with incident energy. For $-t > 1.0$ GeV^2, the Radphi data show significant drop in the differential cross section with increased beam energy, consistent with the trend observed by CLAS between the 3.29 GeV and 3.85 GeV data sets.

9 Conclusions

The purpose of the Radphi experiment is to investigate radiative decays of vector mesons as a probe of meson structure. In particular, the radiative decays of the $\phi(1020)$ to $\gamma a_0(980)$ and $\gamma f_0(980)$ are sensitive to the internal structure of these scalar mesons [9]. Radiative decays to all-neutral final states are advantageous for these studies because they are not contaminated by radiative tails from charged hadronic decay modes. Photoproduction is a favored method for producing vector mesons, but the reconstruction of all-neutral final states in the environment of an electromagnetic beam poses an experimental challenge. The radiative decay $\omega \to \pi^0\gamma$ has a much larger branching ratio of 9%, compared with the 10^{-4} branching ratios of the ϕ to the light scalars, and so provides a starting point for that investigation.

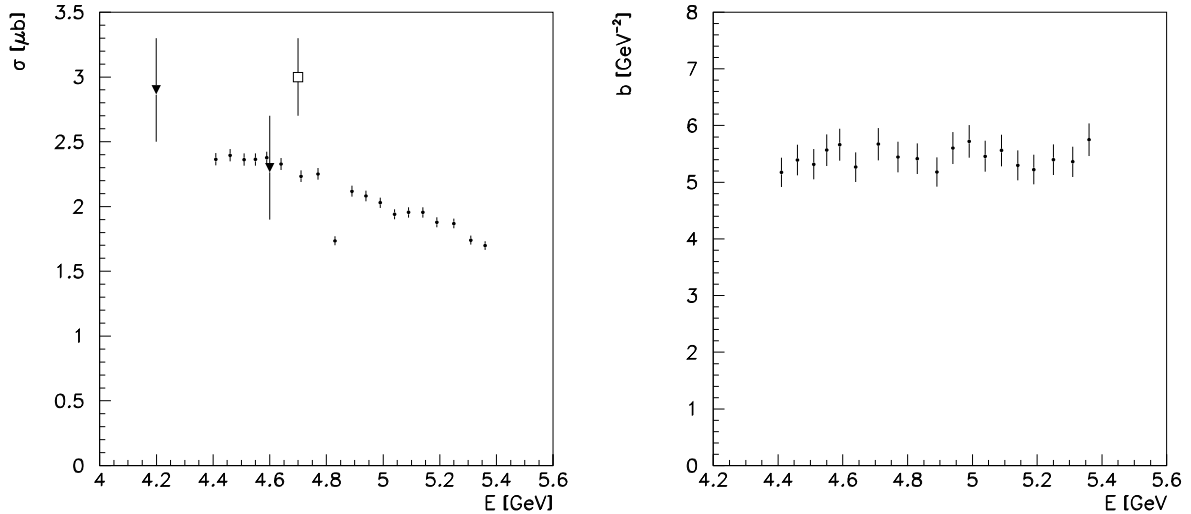Data from the Radphi experiment have been analyzed to examine ω production from the reaction $\gamma p \to \omega p$

Figure 10: The total $\gamma p \to \omega p$ cross section as function of a tagged photon energy (black dots, left panel). The errors bars are estimates of the channel-to-channel normalization uncertainty of 2%. The outlier corresponds to a tagging channel whose timing was misaligned in the on-line trigger. The luminosity for that channel was renormalized in the subsequent analysis to make the cross section for that channel agree with the overall trend in the remaining channels. Measurements from previous experiments are shown for comparison. The right panel shows the slope of the $-t$ distribution as a function of a tagged photon energy.

observed in the decay mode $\omega \to \pi^0 \gamma$. A number of off-line cuts have been devised, together with the tagging analysis, to isolate a very clean ω signal seen in the 3γ invariant mass distribution. The ω yield extracted from the invariant mass distribution has been used to extract a total ω photoproduction cross section on a beryllium target. That cross section can be converted to a $\gamma p \to \omega p$ cross section by multiplying by the atomic number of beryllium, under the assumption that nuclear medium modification effects are negligible. The high statistics of the Radphi data set permit the examination of that assumption over a range from very low to intermediate values of t. The conclusion of this study is that nuclear effects are negligible over this range, with the possible exception of $|t| < 0.1$ GeV^2 where some indication of nuclear suppression relative to the free nucleon cross section is observed.

In order to compare photoproduction from bound protons with that from free protons, it was necessary to account for the momentum distribution of the bound protons in the initial state. For this purpose, a simple spectator model was developed that employed three free parameters to describe the proton in the nuclear medium. Using this model, MC simulations were able to reproduce the distribution of the missing momentum carried away by the unobserved recoil $A = 8$ system.

The Radphi measurement of the ω photoproduction cross section, after non-diffractive contributions are taken out, agrees well with previous measurements. The cross section decreases slowly with increasing beam energy as expected. The shape of the differential cross section $d\sigma/dt$ as a function of $-t$ is also in agreement with previous measurements. It shows the usual exponential drop-off at small $-t < 1.0$ GeV^{-2} and flattening at high $-t > 1.0$ GeV^{-2}. The exponential slope does not depend significantly on energy. The average slope is smaller than previously reported at the Radphi energy but it is consistent with recent measurements at lower energies.

References

[1] "The bremsstrahlung tagged photon beam in Hall B at Jlab", D. I. Sober, *EST LA.*, Nucl. Inst. Meth. A 440 (2000), 263.

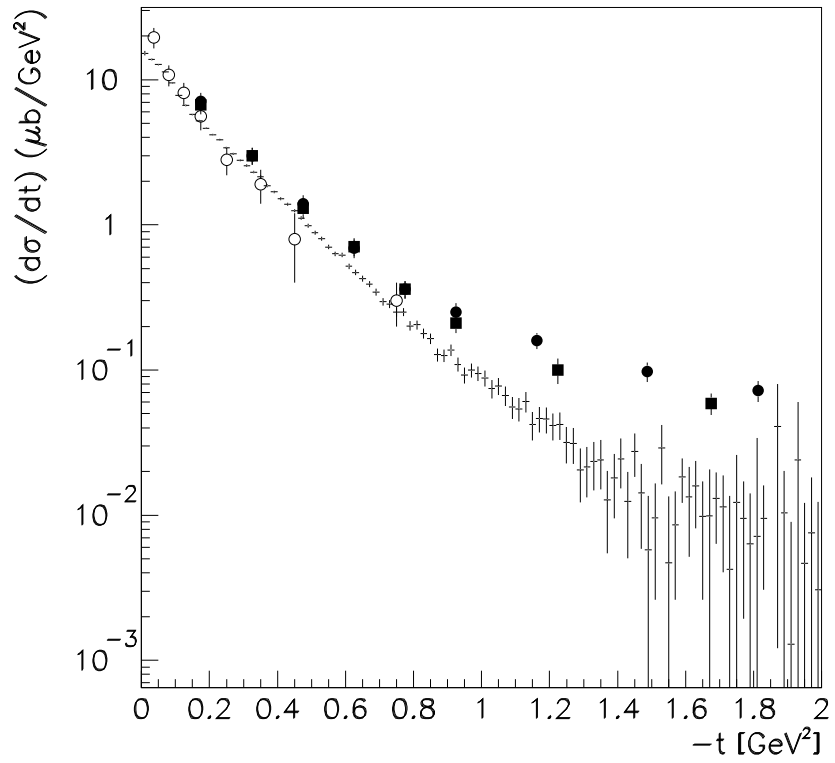[2] "The Radphi detector", R. T. Jones, *et al.*, submitted to Nucl. Inst. Meth. (2004).

Figure 11: Differential cross section for the reaction $\gamma p \to \omega p$ as a function of t. Error bars are statical only. Existing data are shown for comparison, see text for explanation.

[3] "Data Analysis Techniques for High-Energy Physics", R. Fruhwirth *et al.*, Cambridge University Press, 2000

[4] "Monte Carlo study of background from b_1 reactions", M. Kornicer, R. T. Jones, Technical Note radphi-2001-711 (November 2001)

[5] Y. Eisenberg ,*et al.*, Phys. Rev. D **5** (1972) 15.

[6] J. Balls ,*et al.*, Phys. Rev. D **7** (1973) 3150.

[7] M. Batteglieri ,*et al.*, Phys. Rev. Lett **90** (2003) 022002.

[8] D. I. Sober, private communication.

[9] F. E. Close, N. Isgur, and S. Kumano, Nucl. Phys. **B389** (1993) 513.